

## Article

# Enhanced Catalytic Soot Oxidation by Ce-Based MOF-Derived Ceria Nano-Bar with Promoted Oxygen Vacancy

Yu-Chih Tsai <sup>1</sup>, Jechan Lee <sup>2</sup>, Eilhann Kwon <sup>3</sup>, Chao-Wei Huang <sup>4</sup>, Nguyen Nhat Huy <sup>5,6</sup>, Siming You <sup>7</sup>,  
Pei-Syuan Hsu <sup>1</sup>, Wen Da Oh <sup>8,\*</sup> and Kun-Yi Andrew Lin <sup>1,\*</sup>

<sup>1</sup> Department of Environmental Engineering & Innovation and Development Center of Sustainable Agriculture, National Chung Hsing University, Taichung 40227, Taiwan; poi0516tyc@gmail.com (Y.-C.T.); mantau0512@gmail.com (P.-S.H.)

<sup>2</sup> Department of Environmental and Safety Engineering, Ajou University, Suwon 16499, Korea; jlee83@ajou.ac.kr

<sup>3</sup> Department of Environment and Energy, Sejong University, Seoul 05005, Korea; ekwon74@sejong.ac.kr

<sup>4</sup> Department of Chemical and Materials Engineering, National Kaohsiung University of Science and Technology, Kaohsiung 80778, Taiwan; huangcw@nkust.edu.tw

<sup>5</sup> Faculty of Environment and Natural Resources, Ho Chi Minh City University of Technology (HCMUT), Ho Chi Minh City 700000, Vietnam; nnhuy@hcmut.edu.vn

<sup>6</sup> Vietnam National University Ho Chi Minh City, Ho Chi Minh City 700000, Vietnam

<sup>7</sup> James Watt School of Engineering, University of Glasgow, Glasgow G12 8QQ, UK; Siming.You@glasgow.ac.uk

<sup>8</sup> School of Chemical Sciences, Universiti Sains Malaysia, Georgetown 11800, Malaysia

\* Correspondence: ohwenda@usm.my (W.D.O.); linky@nchu.edu.tw (K.-Y.A.L.)



**Citation:** Tsai, Y.-C.; Lee, J.; Kwon, E.; Huang, C.-W.; Huy, N.N.; You, S.; Hsu, P.-S.; Oh, W.D.; Lin, K.-Y.A. Enhanced Catalytic Soot Oxidation by Ce-Based MOF-Derived Ceria Nano-Bar with Promoted Oxygen Vacancy. *Catalysts* **2021**, *11*, 1128.

<https://doi.org/10.3390/catal11091128>

Academic Editor: Min Kim

Received: 30 July 2021

Accepted: 7 September 2021

Published: 18 September 2021

**Publisher's Note:** MDPI stays neutral with regard to jurisdictional claims in published maps and institutional affiliations.



**Copyright:** © 2021 by the authors. Licensee MDPI, Basel, Switzerland. This article is an open access article distributed under the terms and conditions of the Creative Commons Attribution (CC BY) license (<https://creativecommons.org/licenses/by/4.0/>).

**Abstract:** As CeO<sub>2</sub> is a useful catalyst for soot elimination, it is important to develop CeO<sub>2</sub> with higher contact areas, and reactivities for efficient soot oxidation and catalytic soot oxidation are basically controlled by structures and surface properties of catalysts. Herein, a Ce-Metal organic framework (MOFs) consisting of Ce and benzene-1,3,5-tricarboxylic acid (H<sub>3</sub>BTC) is employed as the precursor as CeBTC exhibits a unique bar-like high-aspect-ratio morphology, which is then transformed into CeO<sub>2</sub> with a nanoscale bar-like configuration. More importantly, this CeO<sub>2</sub> nanobar (CeONB) possesses porous, and even hollow structures, as well as more oxygen vacancies, enabling CeONB to become a promising catalyst for soot oxidation. Thus, CeONB shows a much higher catalytic activity than commercial CeO<sub>2</sub> nanoparticle (comCeO) for soot oxidation with a significantly lower ignition temperature (T<sub>ig</sub>). Moreover, while soot oxidation by comCeO leads to production of CO together with CO<sub>2</sub>, CeONB can completely convert soot to CO<sub>2</sub>. The tight contact mode also enables CeONB to exhibit a very low T<sub>ig</sub> of 310 °C, whereas the existence of NO also enhances the soot oxidation by CeONB to reduce the T<sub>ig</sub>. The mechanism of NO-assisted soot oxidation is also examined, and validated by DRIFTS to identify the formation and transformation of nitrogen-containing intermediates. CeONB is also recyclable over many consecutive cycles and maintained its high catalytic activity for soot oxidation. These results demonstrate that CeONB is a promising and easily prepared high-aspect-ratio Ce-based catalyst for soot oxidation.

**Keywords:** MOFs; ceria; carbon black; catalytic oxidation; high aspect ratio

## 1. Introduction

While diesel engines are widely used because of several advantages, namely, relatively low operation cost, relatively high durability, and energy efficiency, pollutants from diesel engines, such as NO<sub>x</sub> and soot, have threatened public health. Specifically, soot is even considered as a toxic contaminant in view of its carcinogenicity [1]; thus, it is critical to prevent emission of soot into the environment. To this end, diesel particulate filters (PDFs) have been frequently adopted to remove soot particles from the exhaust emission of diesel engines, and soot collected inside PDFs must be then decomposed in order to regenerate PDFs. Consequently, catalytic decomposition of soot has been regarded as a key step for

eliminating soot [2–5], and catalysts for soot oxidation at lower temperatures and higher reaction rates are then highly crucial [2].

Up to date, several transition metal oxides, including Ce, Co, Mn, Fe, Cu, V, and Mo [6–15], have been demonstrated as catalysts to decompose soot. Ce, especially CeO<sub>2</sub>, has become a particularly attractive catalyst for soot oxidation as CeO<sub>2</sub> exhibits a relatively high oxygen storage capacity via the redox cycle between Ce<sup>4+</sup> and Ce<sup>3+</sup> for reversibly adding/removing oxygen, making CeO<sub>2</sub> possess high catalytic activities [1,16]. Thus, CeO<sub>2</sub> has been increasingly studied for soot oxidation recently. Nevertheless, since catalytic soot oxidation is dominantly controlled by their configurations, and surface properties [17–19], it would be useful to construct CeO<sub>2</sub> with higher contact areas, and higher reactivities for effective soot oxidation [19–22]. Especially, high-aspect-ratio configurations, such as fibrous, rod-like, or bar-like structures, have been validated as promising shapes to offer high contact surfaces per volume, and more accessible reactive sites [23,24].

Moreover, catalysts with more reactive surfaces (i.e., more oxygen vacancies) have also been proven to enhance catalytic oxidation applications as oxygen vacancies can accelerate the diffusion rate of oxygen and promote oxygen mobility for improving soot oxidation [1,25]. Thus, it would be essential to establish high-aspect-ratio CeO<sub>2</sub> with more porous structures, and more oxygen vacancies for catalytic soot oxidation.

As high-aspect-ratio metal oxides conventionally require complicated protocols, such as electrospinning techniques, alternative metal-coordinated networks with certain structures have been increasingly utilized as templates which are then converted to metal oxides with desired configurations via thermal treatments [14,26]. In particular, metal organic frameworks (MOFs) have been increasingly adopted as the precursor templates as they can be designed to afford high-aspect-ratio morphologies which would be then converted to high-aspect-ratio metal oxides with promoted oxygen vacancies [14,27–29]. Therefore, Ce-based MOFs with bar-like nanoscale morphologies can be promising templates for preparing nanobar (NB)-like CeO<sub>2</sub> with more oxygen vacancies as advantageous catalysts to oxidize soot.

However, very few studies have been conducted for examining such NB-like CeO<sub>2</sub> with well-defined configurations derived from MOFs for soot oxidation. More importantly, there is almost no study discussing how such a MOF-derived NB-like CeO<sub>2</sub> (CeONB) is different from typical CeO<sub>2</sub> material in terms of physical/chemical properties, oxygen vacancy, and catalytic behaviors for soot oxidation. Therefore, the aim of this study focuses on direct comparisons between Ce-MOFs-derived CeONB and commercial CeO<sub>2</sub> nanoparticle (comCeO) for catalytic soot oxidation for probing into the structure–property–reactivity relationship of this MOF-derived NB-like CeO<sub>2</sub> to evaluate effects of morphologies and oxygen vacancies on soot oxidation. Specifically, a Ce-MOF consisting of Ce and benzene-1,3,5-tricarboxylic acid (BTC) is employed as the precursor as the coordinated framework of CeBTC exhibits a unique NB-like configuration. Through one-step calcination, this NB-like CeBTC is converted CeO<sub>2</sub> with a NB structure consisting of many CeO<sub>2</sub> nanoparticles, as illustrated in Figure 1. More importantly, CeONB exhibits hollow structures, and also more oxygen vacancies, enabling CeONB to become a promising catalyst for soot oxidation.

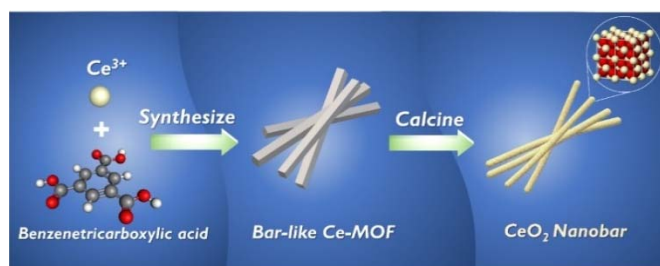


**Figure 1.** Scheme for preparing bar-like CeO<sub>2</sub> from Ce-MOF.

## 2. Results and Discussion

### 2.1. Characterization of CeONB

Since CeONB was derived from CeMOF comprised of  $\text{Ce}^{4+}$  and  $\text{H}_3\text{BTC}$ , the morphology of CeMOF was visualized in Figure 2a, in which a typical bar (or rod)-like shape can be detected. The length of these bar-like CeMOF ranged from sub-micrometer to a few micrometers with relatively high aspect ratios and smooth surfaces. The crystalline structure of this CeMOF could also be indexed to the reported XRD pattern of this CeMOF (i.e., CeBTC [30]), indicating that the coordination of  $\text{Ce}^{3+}$  and BTC can afford the bar-like morphology of MOF.

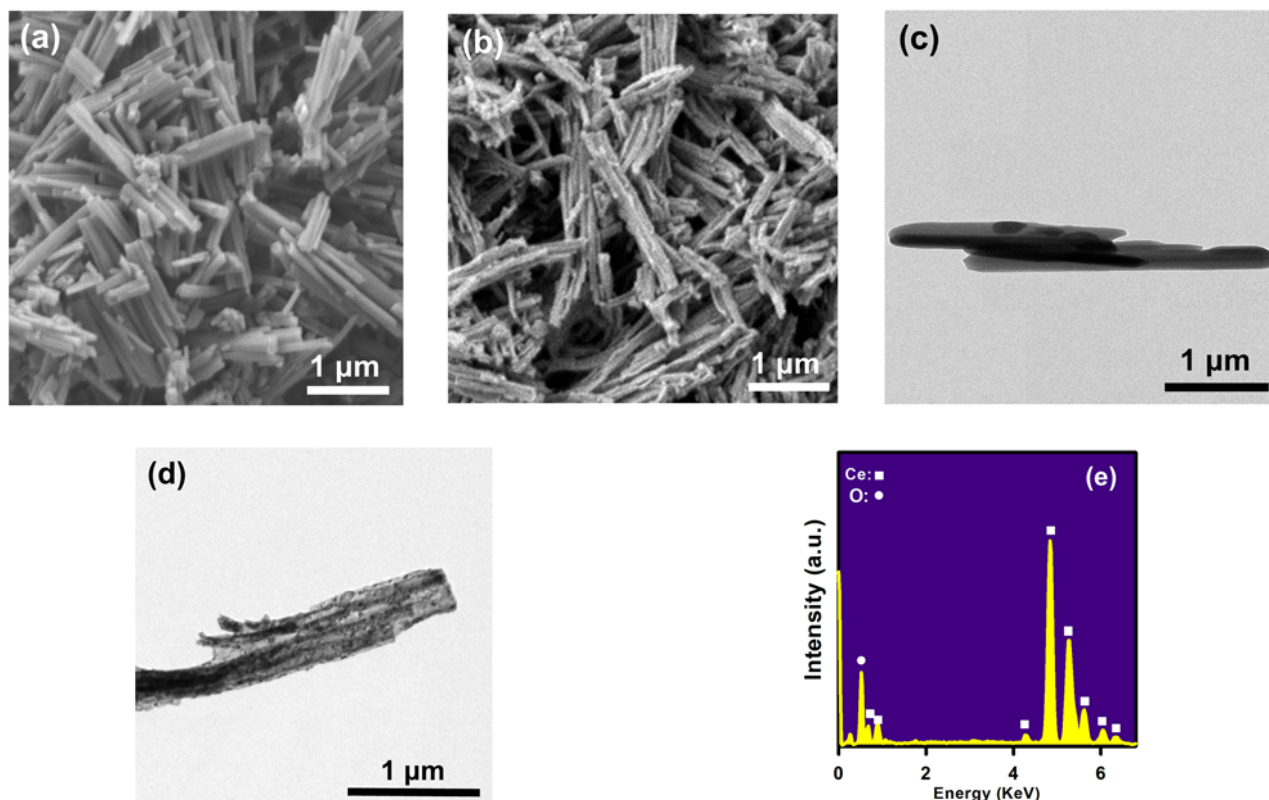


**Figure 2.** (a) SEM image of bar-like Ce-MOF, (b) SEM image of  $\text{CeO}_2$  nanobar (CeONB)-derived from Ce-MOF, (c) TEM image of Ce-MOF, and (d) CeONB; (e) EDS analysis.

After calcination of this CeMOF, the resulting product can be seen in Figure 2b, in which the bar-like morphology could be still observed with relatively high aspect ratios. The dimensions of these bar-like products were also similar to those of the CeMOF precursor. Nevertheless, the resulting product exhibited significantly roughened surfaces. In addition, these products seemed slightly slimmer than the precursor CeMOF, possibly because the calcination process had decomposed the organic ligand (i.e., BTC), leaving metal oxides. Its EDS spectrum (Figure 2e) also showed significant signals of Ce, and O without other noticeable elements, demonstrating that the resultant product from calcination of Ce-MOF should only consist of Ce, and O.

On the other hand, Figure 2c,d also reveal TEM images of Ce-MOF, and its calcined product, respectively. As the TEM image of Ce-MOF indicated that Ce-MOF was bar-like, solid, and smooth, the TEM image of the calcimined product was also bar-like but semi-transparent with non-homogeneous surfaces. These features were in line with the observation seen in the SEM images of the calcined product of Ce-MOF.

Closer views (Figure 3a,b) further reveal that the bar-like configuration of the calcined product in fact consisted of many fine NPs (with sizes of a few tens nanometers). More

importantly, the non-homogeneous texture of the calcined product also unveiled that the calcined product contained voids (e.g., hollow structures) and pores, suggesting that the calcination process not only decomposed the organic ligand but also enabled the formation of special structures. The lattice-resolved HRTEM (Figure 3c) also displays d-spacing of 0.312 and 0.191 nm which correspond to the (110) and (220) planes of  $\text{CeO}_2$ , indicating that these bar-like product were comprised of crystallized  $\text{CeO}_2$ . The SAED pattern displayed as Figure 3d can also be well indexed to the polycrystalline feature of  $\text{CeO}_2$ . Figure 4a further displays the crystalline structure of CeONB, which was considerably different from that of Ce-MOF, validating that Ce-MOF had been transformed after calcination, and the XRD pattern of this CeONB could be well-indexed to a cubic fluorite-type  $\text{CeO}_2$  according to JCPDS Card No. 43-1002.

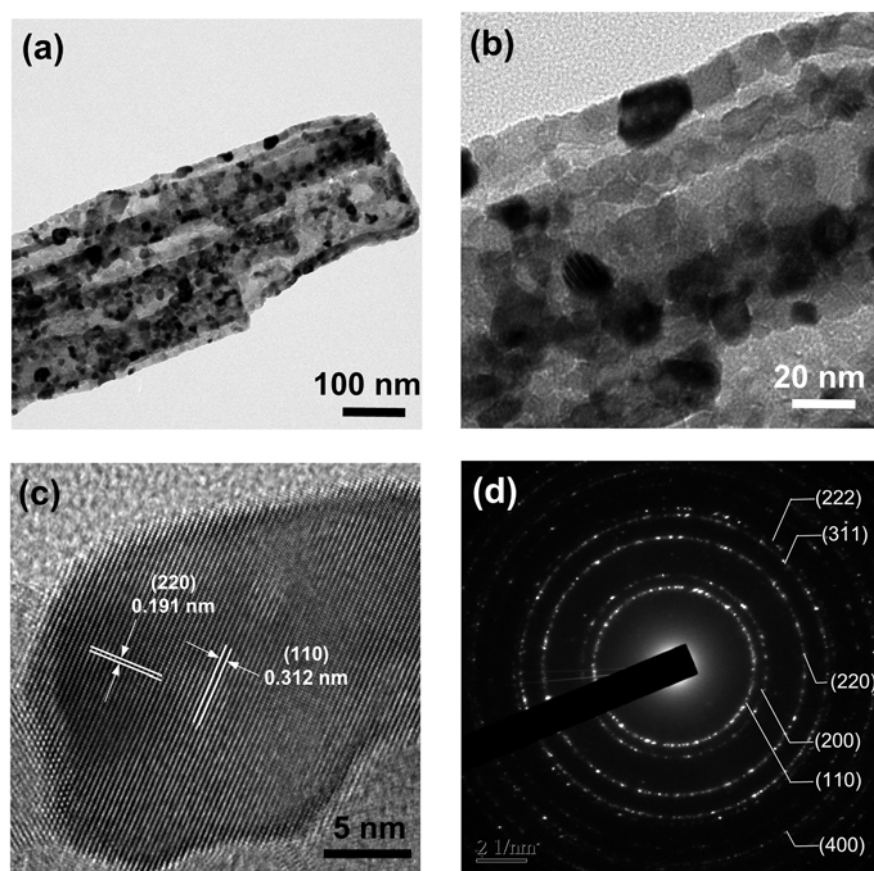


**Figure 3.** (a,b) TEM image of Ce-MOF under various magnifications, (c) lattice-resolved image of CeONB and (d) SAED pattern of CeONB.

On the other hand, as comCeO was intentionally employed as a reference material here for comparisons with this CeONB, the SEM image of comCeO had also been visualized in Figure S1a,b. In particular, Figure S1b clearly indicates that comCeO comprised of many fine particles with sizes of 50–100 nm. However, these NPs of comCeO agglomerated, forming sub-microscale sheets. The XRD pattern of comCeO had also been added to Figure 4a, and it was also well-indexed to the cubic fluorite-type  $\text{CeO}_2$ . These images had unveiled that the CeMOF-derived CeONB certainly exhibited a rather different morphology from comCeO.

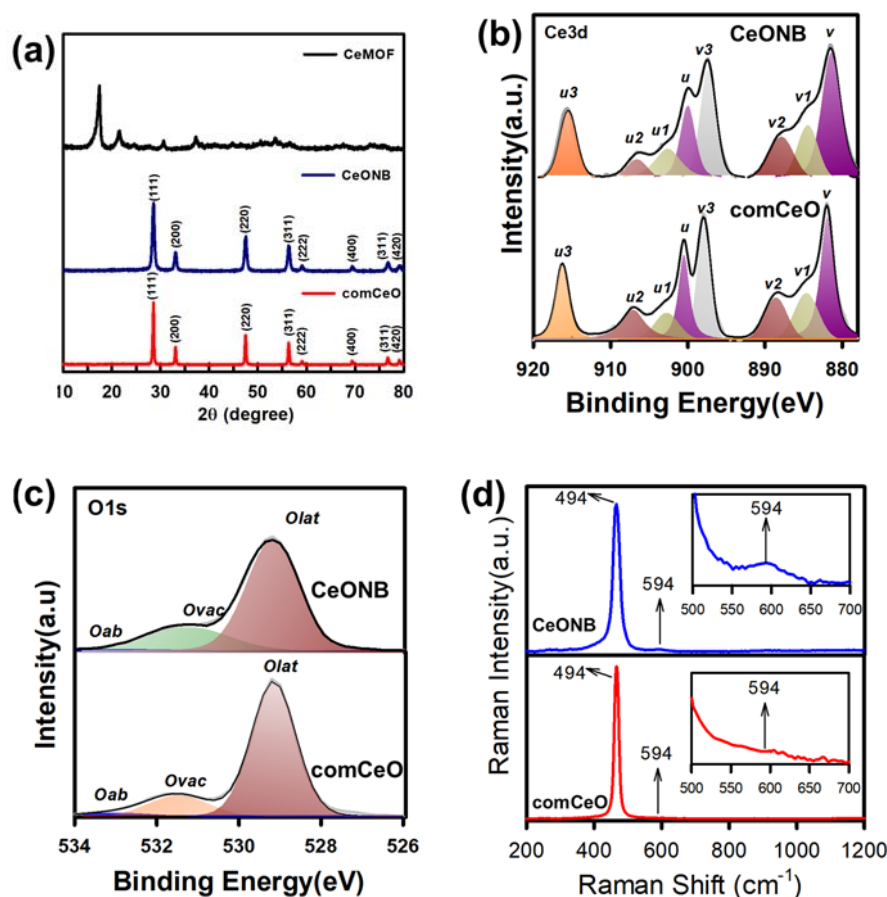


**Figure 4.** (a) XRD patterns of Ce–MOF, CeONB, comCeO; and XPS analyses of CeONB and comCeO: (b) Ce3d and (c) O1s; (d) Raman spectra of CeONB and comCeO.

Moreover, the surface chemistry of CeONB was analyzed by XPS, and its Ce3d core-level spectrum can be seen in Figure 4b, which could be deconvoluted to reveal eight peaks. These underlying peaks labelled with *v* and *u* can be ascribed to Ce3d<sub>3/2</sub> and Ce3d<sub>5/2</sub>, respectively. In particular, the peaks tagged with *v*, *v*<sub>2</sub>, *v*<sub>3</sub> and *u*, *u*<sub>2</sub>, *u*<sub>3</sub> corresponded to Ce<sup>4+</sup>, whereas the peaks labelled by *v*<sub>1</sub> and *u*<sub>1</sub> were attributed to Ce<sup>3+</sup> [31]. The XPS analysis of comCeO was also conducted, and its Ce3d spectrum can be displayed in Figure 4b, which reveals the same eight peaks after deconvolution.

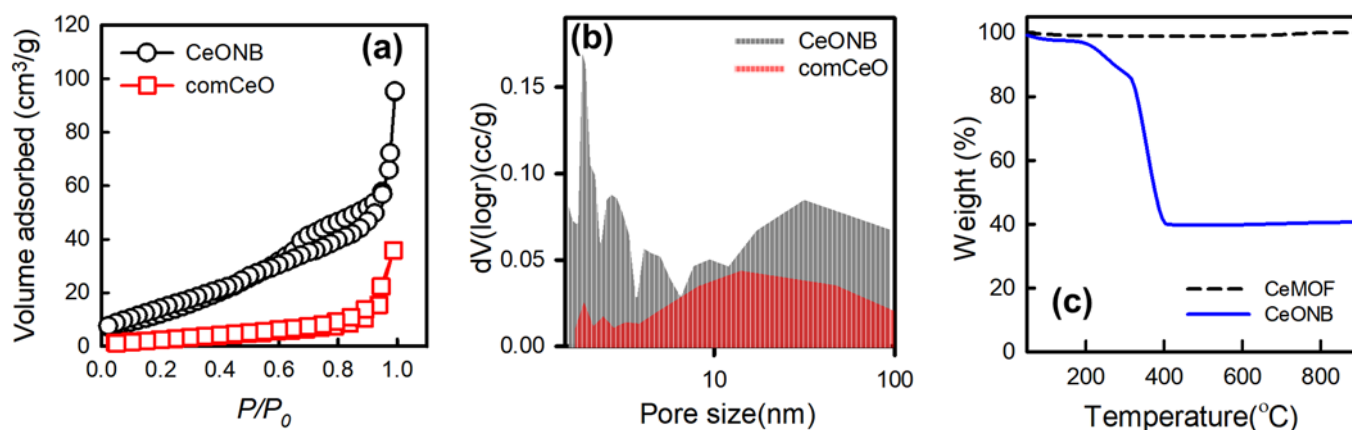
To compare differences between CeONB and comCeO, the peak area ratios of Ce<sup>3+</sup> / (Ce<sup>3+</sup> + Ce<sup>4+</sup>) of these two materials were then quantified, as this Ce<sup>3+</sup> / (Ce<sup>3+</sup> + Ce<sup>4+</sup>) ratio could be related to surface catalytic properties [31]. As summarized in Table 1, the concentration of Ce<sup>3+</sup> in CeONB was 20.5% noticeably higher than that of comCeO (16.2%). This indicates that comCeO possessed a higher degree of crystallinity, and thus contained a lower extent of oxygen vacancy. Moreover, the O1s core-level spectra of these two CeO<sub>2</sub> materials were also measured (Figure 4c). Both of these spectra could be deconvoluted into three peaks, attributed to lattice oxygen (O<sub>lat</sub>), oxygen vacancy (O<sub>vac</sub>), and adsorbed oxygen species (O<sub>ab</sub>), respectively [32,33]. The concentration of O<sub>vac</sub> of CeONB accounted for 23.7%, which was substantially higher than that of comCeO (i.e., 16.4%). This result demonstrated that CeONB exhibited a much higher extent of oxygen vacancy than comCeO. These results also indicate that this Ce-MOF-derived CeONB not only showed a different structure (i.e., high aspect ratio, porous, and hollow) from comCeO, but also exhibited distinct surface properties from comCeO with a higher extent of oxygen vacancy.

**Table 1.** Property analyses of CeONB and comCeO.

Catalyst	(Ce <sup>3+</sup> /(Ce <sup>3+</sup> + Ce <sup>4+</sup> ))	O <sub>vac</sub> /(O <sub>lat</sub> + O <sub>vac</sub> + O <sub>ab</sub> )	I <sub>D</sub> /I <sub>F2g</sub>
CeONB	20.5%	23.7%	1.2%
comCeO	16.5%	16.4%	0.4%

Moreover, Raman spectra of CeONB and comCeO were also measured to further examine their surface structure in Figure 4d. Both CeONB and comCeO showed a tall peak at 464 cm<sup>-1</sup>, corresponding to the F<sub>2g</sub> mode of the fluorite-type structure of CeO<sub>2</sub> [32]. On the other hand, a short peak could also be noticed at 594 cm<sup>-1</sup>, which was correlated to the formation of oxygen vacancy (denoted as I<sub>D</sub>) [29]. The intensity ratio of I<sub>D</sub> over I<sub>F2g</sub> was adopted to determine the relative concentration of oxygen vacancy. Thus, the ratios of I<sub>D</sub> over I<sub>F2g</sub> of CeONB and comCeO were calculated and listed in Table 1. CeONB possessed a higher ratio of I<sub>D</sub>/I<sub>F2g</sub> (i.e., 1.2%) than comCeO (i.e., 0.4%), suggesting that CeONB exhibited a higher extent of oxygen vacancy than comCeO.

Additionally, as CeONB exhibited a bar-like morphology with the porous and hollow structure, its textural properties were then measured. Figure 5a shows that the N<sub>2</sub> sorption isotherm of CeONB can be categorized as the IUPAC type VI isotherm as it contained a small hysteresis loop attributed to porous structures. The pore size distribution (Figure 5b) validated that CeONB exhibited the porous structure, including mesopores. The corresponding surface area was then quantified as 55 m<sup>2</sup>/g, and pore volume was 0.14 cm<sup>3</sup>/g. Besides, the N<sub>2</sub> sorption isotherm of comCeO was also obtained, and its N<sub>2</sub> sorption amount was significantly much lower than that of CeONB as the surface area of comCeO was only 10 m<sup>2</sup>/g, and the total pore volume was 0.05 cm<sup>3</sup>/g. This pronounced difference demonstrated that CeONB exhibited a much higher surface area owing to its high aspect ratio and porous structure, whereas comCeO, even though consisting of NPs, was seriously agglomerated.

**Figure 5.** (a) N<sub>2</sub> sorption isotherms, and (b) pore size distributions of CeONB and comCeO; (c) TGA analyses of CeMOF, and CeONB.

Even though CeONB was shown to exhibit more superior textural characteristics than comCeO, the textural characteristics were not the only parameter controlling catalytic activities. Therefore, chemisorption analysis was then conducted to offer more direct insights into catalytic activities of these catalysts. Before implementing chemisorption analysis, a TGA curve of CeONB was first obtained and displayed in Figure 5c to evaluate its thermal stability. CeONB was almost unchanged through the heating process up to 900 °C, demonstrating that CeONB was highly thermally stable. Besides, since CeONB was derived from CeMOF, and thus the TGA curve of CeMOF was also measured, and CeMOF started decomposition at around 200 °C, and gradually decomposed until 390 °C to eliminate organic components, leaving a residual weight ~40%. This suggests that the conversion of CeMOF to CeONB was around 40 wt.%.

Subsequently, the TPR profiles of CeONB and comCeO were determined and displayed in Figure 6a. CeONB showed two notable reduction peaks at 520 °C (labelled as “a”) and 765 °C (labelled as “b”), corresponding to the reduction in CeO<sub>2</sub> at the surface region, and the reduction in the bulk CeO<sub>2</sub>, respectively. Nevertheless, the peak intensity of “a” in comCeO was considerably lower than that of CeONB, and the peak intensity of “b” in comCeO also appeared at a much higher temperature (800 °C). These comparisons suggested that CeONB exhibited a much higher extent of reducibility than comCeO. As soot oxidation is strongly related to reducibility of catalysts [1], this result indicated that CeONB would be a much more advantageous catalyst for soot oxidation.

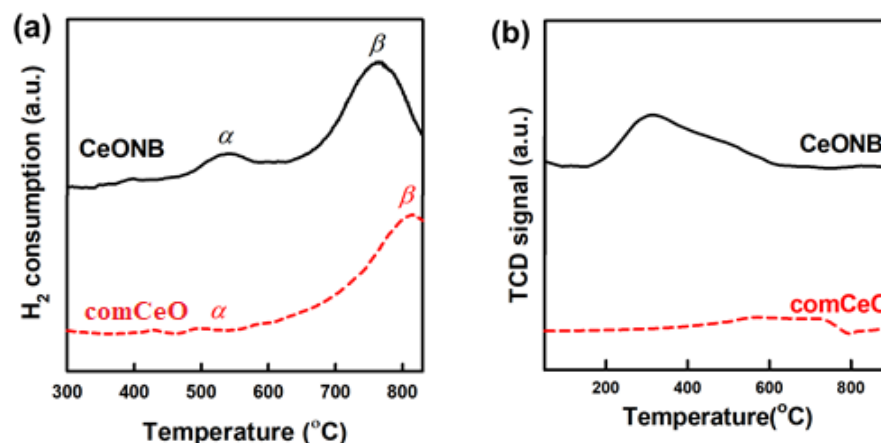


Figure 6. (a) TPR profiles, and (b) TPD-O<sub>2</sub> profiles of CeONB and comCeO.

Besides, TPD-O<sub>2</sub> has also been an insightful tool to examine catalytic activities especially because TPD-O<sub>2</sub> would offer useful information about the surface and bulk oxygen species of catalysts [34]. Figure 6b displays the desorption region from 150–900 °C. In the case of CeONB, it exhibited a noticeable desorption peak starting from 180 °C with a peak center at 295 °C. Nevertheless, comCeO did not exhibit any notable peaks below 600 °C. Since the oxygen desorbed in the range of 100–300 °C would be ascribed to physisorbed and/or chemisorbed oxygen molecules on surfaces, these TPD-O<sub>2</sub> profiles suggested that CeONB possessed a higher amount of chemisorbed oxygen which shall enable CeONB to exhibit a higher catalytic activity [34].

Moreover, oxygen desorbed in the range of 550–900 °C would be correlated to migration of lattice oxygen of catalysts. Although both CeONB and comCeO exhibited desorbed oxygen in this particular temperature range, CeONB showed a much larger amount of desorption of oxygen than comCeO. This suggests that the degree of migration of lattice oxygen in CeONB seemed more intense than that in comCeO, suggesting a higher degree of oxygen vacancy in CeONB.

## 2.2. Soot Oxidation by CeONB and Commercial CeO<sub>2</sub> NPs

In this study, a fixed-bed tubular reactor was employed to conduct soot oxidation experiments, in which the soot oxidative activity of CeONB was evaluated by temperature-programmed oxidation (TPO). Various parameters (e.g., T<sub>ig</sub>, T<sub>m</sub>, T<sub>50</sub>, T<sub>90</sub>, and T<sub>e</sub>) were performed to measure the catalytic activities of CeO<sub>2</sub>. In particular, T<sub>ig</sub> was the ignition temperature of catalytic soot oxidation; T<sub>50</sub> and T<sub>90</sub> represented the temperatures of the soot oxidation at 50% and 90%, respectively; and T<sub>m</sub> was denoted as the temperature-programmed oxidation temperature at the highest CO<sub>2</sub> concentration. Then, the CO<sub>2</sub> selectivity (S<sub>CO2</sub>) was calculated via  $S_{CO_2} = (C_{CO_2} / (C_{CO} + C_{CO_2})) \times 100\%$ , where C<sub>CO2</sub> and C<sub>CO</sub> denote the outlet concentration of CO<sub>2</sub> and CO, respectively. In particular, S<sub>mCO2</sub> denotes the S<sub>CO2</sub> at T<sub>m</sub>.

Before investigating catalytic activities of CeONB for soot oxidation, the TPO profile of soot oxidation in absence of any catalysts was measured as a reference line. As shown in

Figure 7a, in the absence of catalysts, the  $T_{ig}$  of soot oxidation was 490 °C and  $S_{CO_2}$  was 35.1% (Figure 7b), suggesting that the oxidation of bare soot initiated at a relatively high temperature whereas an un-desired by-product, namely CO, was produced during the soot oxidation. Nevertheless, when CeONB was introduced, the corresponding  $T_{ig}$  was significantly reduced from 490 °C to 352 °C with 100% of  $S_{CO_2}$ , revealing that CeONB can enhance catalytic soot oxidation with the outstanding  $CO_2$  conversion efficiency.

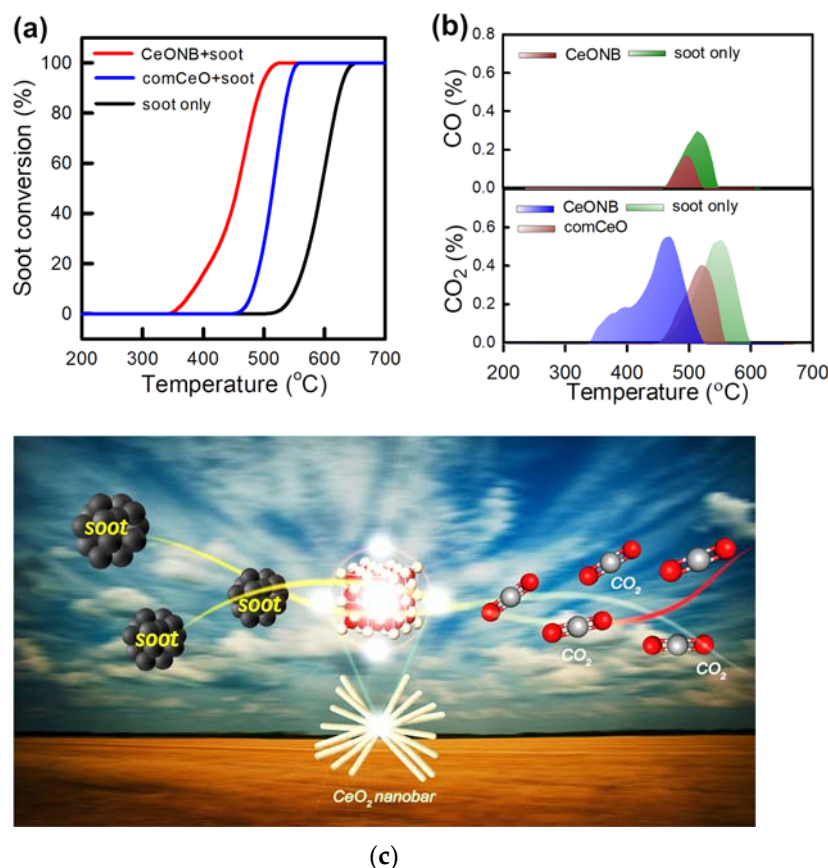


**Figure 7.** Soot oxidation by CeONB and comCeO: (a) soot conversion (%) under the loose contact mode and (b) concentrations of CO, and CO<sub>2</sub> during soot oxidation; (c) illustration of selective soot oxidation by CeONB.

Additionally, comCeO was also used to catalyze soot oxidation, and its  $T_{ig}$  (461 °C) was also substantially lower than 490 °C but it was still much higher than that of CeONB. This signified that CeONB would exhibit a higher catalytic activity than comCeO for soot oxidation possibly because CeONB showed the larger surface area in contact with soot particles than comCeO. Besides, CeONB also possessed more superior redox properties and higher extent of surface oxygen vacancies than comCeO, thereby improving intrinsic activities for soot oxidation [35]. More importantly, Figure 7b also reveals that, while comCeO was able to convert soot completely with 100% conversion, CO was co-generated with CO<sub>2</sub> during soot oxidation with  $S_{CO_2} = 73.8\%$ . As no CO was produced from soot oxidation by CeONB, CeONB certainly exhibited more favorable and efficient catalytic activities for soot oxidation than comCeO.

To further distinguish catalytic activities of CeONB and comCeO, activation energy ( $E_a$ ) of soot oxidation by CeONB and comCeO were further determined by the Coats–Redfern integral method [36]. Thus, plots of  $\ln[\ln(1 - \alpha)/T^2]$  vs.  $1/T$  of soot oxidation

under different conditions were obtained using TGA, and  $\alpha$  denotes the reaction extent or conversion quantified via the equation:

$$\alpha = (m_0 - m_t)/(m_0 - m_\infty) \quad (1)$$

where  $m_0$ ,  $m_t$ , and  $m_\infty$  are the initial mass, the mass in time  $t$ , and the mass at the end of the reaction, respectively. Based on TGA curves of various cases as seen in Figure 8a, their corresponding plots of  $\ln[\ln(1 - \alpha)/T^2]$  vs.  $1/T$  are displayed in Figure 8b. The data points were then fitted by the linear regression, and fitting correlation coefficients ( $R^2$ ) of the fitted lines were all larger than 0.99. Accordingly, the activation energies ( $E_a$ ) of these three cases were then calculated as shown in Figure 8b. As the  $E_a$  of soot oxidation in the absence of catalysts was 189.2 kJ/mol (Table 2), the  $E_a$  values of soot oxidation can be significantly reduced to 155.1 and 101.5 kJ/mol by comCeO, and CeONB, respectively. This clearly demonstrated that CeONB exhibited a considerably higher catalytic activity than comCeO for soot oxidation.

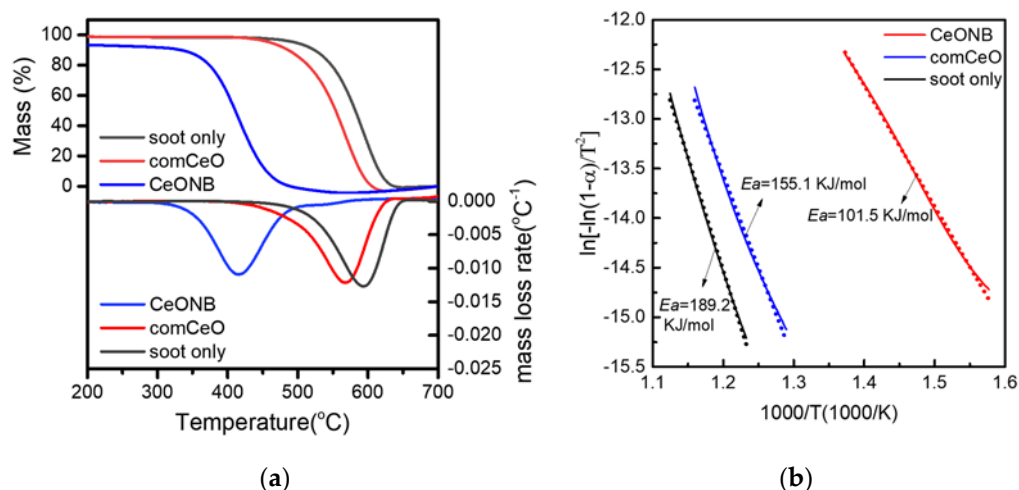


**Figure 8.** (a) TG-DTG curves of soot with, and without catalysts; (b) Fitting curves of  $\ln[-\ln(1 - \alpha)/T^2]$  vs.  $1/T$ .

**Table 2.** Kinetic parameters of soot oxidation by the Coast-Redfern method.

Catalyst	$0.15 \leq \alpha \leq 0.9$	$E_a$ , KJ/mol	A, 1/S	$R^2$
Soot only	538~616 °C	189.2	$1.44 \times 10^9$	0.997
comCeO	502~589 °C	155.1	$6.65 \times 10^7$	0.993
CeONB	361~455 °C	101.5	$3.75 \times 10^6$	0.999

For further evaluating the competence of CeONB, Table 3 lists the data of soot oxidation by reported Ce-containing catalysts reported in the literature. Compared to the other reported catalysts, CeONB certainly showed relatively low values of  $T_{ig}$ ,  $T_{10}$ ,  $T_{50}$ , and  $T_{90}$ . This verified that the catalytic activity of CeONB not only surpassed comCeO but also many other Ce-containing catalysts, confirming that CeONB was an advantageous and promising catalyst for soot oxidation.

**Table 3.** Soot conversion by CeONB and other Ce-related catalysts.

Catalyst	Contact	T <sub>10</sub>	T <sub>50</sub>	T <sub>90</sub>	T <sub>ig</sub>	T <sub>m</sub>	T <sub>e</sub>	S <sub>CO2</sub>	Reference
CeONB	loose	384	456	494	352	467	526	100%	This work
	tight	354	388	423	310	393	456	100%	This work
CeONB (+NO)	loose	329	363	398	300	364	432	100%	This work
Commercial CeO <sub>2</sub>	loose	482	514	540	461	520	560	73.8%	This work
CeO <sub>2</sub> NR	tight	372	394	450	-	387	-	-	[30]
SCS	loose	483	562	-	-	562	-	-	[31]
	tight	358	411	-	-	417	-	-	[31]
SA-stars	loose	435	543	-	-	552	-	-	[31]
	tight	354	410	-	-	403	-	-	[31]
Ce-NC	loose	417	477	584	-	-	622	-	[21]
	tight	396	400	425	-	-	618	-	[21]
CeO <sub>2</sub> NR	loose	429	536	623	-	-	656	-	[21]
	tight	381	416	455	-	-	625	-	[21]
Ce-NC/ZSM-5	loose	394	525	590	-	-	620	-	[21]
	tight	335	439	481	-	-	576	-	[21]
Ce-M	loose	398	538	604	-	-	630	-	[21]
	tight	374	564	510	-	-	590	-	[21]
Ce-SCS	loose	436	580	633	-	-	670	-	[21]
	tight	392	476	558	-	-	638	-	[21]
CeO <sub>2</sub>	tight	379	448	-	-	-	-	97%	[32]
CeO <sub>2</sub> (+NO)	tight	351	422	-	-	-	-	92%	[32]
CeO <sub>2</sub> -co	tight	381	460	-	-	-	-	93%	[32]
CeO <sub>2</sub> -co(+NO)	tight	356	430	-	-	-	-	87%	[32]
MnCe	tight	304	375	-	-	-	-	100%	[32]
MnCe (+NO)	tight	300	358	-	-	-	-	98%	[32]

### 2.3. Effect of Tight Contact and Loose Contact Conditions on Soot Oxidation by CeONB

As the contact modes between catalysts and soot particles may influence the soot oxidation efficiencies, two particular modes (i.e., the loose contact and tight contact) were further investigated. In the loose contact mode, it is considered as a mixture of catalyst and soot in the practical condition, where shapes and appearance of catalysts would significantly influence soot oxidation for providing insights into essence of catalyst–soot contact. On the other hand, the tight contact modes, i.e., intimate contacts between soot and catalysts, elucidated intrinsic activities of catalysts and was not restricted by poor soot–catalyst contact. The TPO profiles of two contact modes from soot oxidation by CeONB were illustrated as displayed in Figure 9a. It can be noted that, though  $S_{mCO_2}$  from two modes could be achieved 100%, the tight contact mode certainly improved TPO profile remarkably as its corresponding  $T_{ig}$  and  $T_{50}$  were 310 and 388 °C, which were comparatively lower than that of the loose contact (i.e., 352 and 456 °C), respectively.

Besides, to further distinguish the difference between these contact modes,  $T_{50}$  values of these two contact modes were analyzed as displayed in Figure 9b. It can also be seen that, while both contact modes exhibited  $S_{mCO_2} = 100\%$  (Figure 9c),  $T_{50}$  of loose contact mode was relatively higher than that of the tight contact mode. These results indicated that the soot oxidation efficiency by CeONB was considerably improved under the tight contact mode in comparison with the loose contact one. This could be attributed to the fact that the intimate interfacial contact between CeONB and soot particles could be achieved under the tight contact mode whereas much less contact between two reactants could be afforded by the loose contact counterpart [34].

For comparison, comCeO was also employed for soot oxidation under two contact modes. It can be noted that soot oxidation was notably enhanced by comCeO under the tight contact mode as the corresponding  $T_{50}$  was only 476 °C, which was lower than that of the loose contact mode, further suggesting the positive effect of the tight contact mode to the soot oxidation. Nonetheless, the soot oxidation efficiency of comCeO was still much less

effective than CeONB for soot oxidation even under the tight contact mode, illustrating that CeONB possessed intrinsically higher catalytic activity than comCeO for soot oxidation.

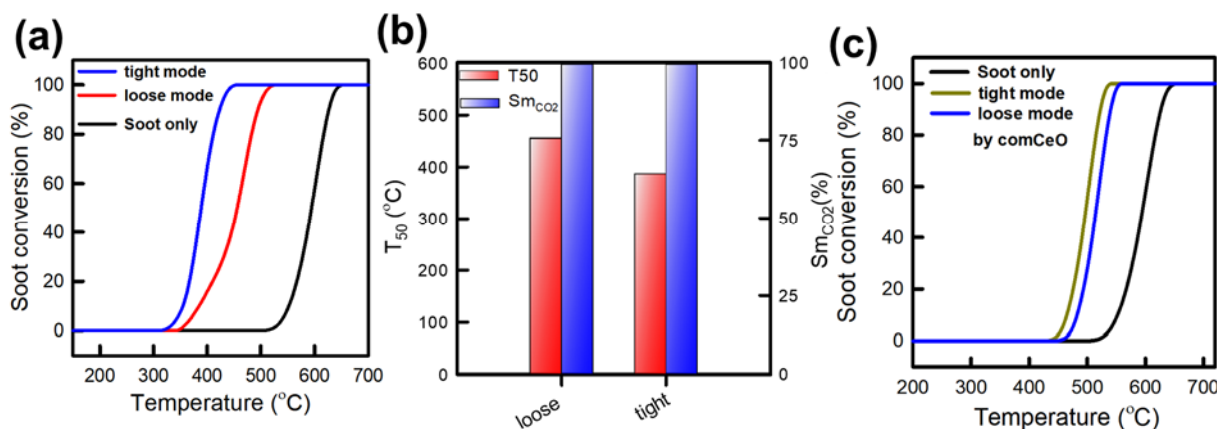


**Figure 9.** Soot oxidation by CeONB under the loose contact and tight contact modes: (a) soot conversion (%), (b)  $T_{50}$  and  $S_{mCO_2}$ , and (c) soot oxidation by comCeO under the loose contact and tight contact modes.

#### 2.4. Effect of NO on Soot Oxidation by CeONB

Since feed gases would also consist of other components, such as  $NO_x$ , it would be important to further examine the effect of NO on soot oxidation by CeONB. Figure 10a displays TPO profiles of soot oxidation with and without the existence of NO.

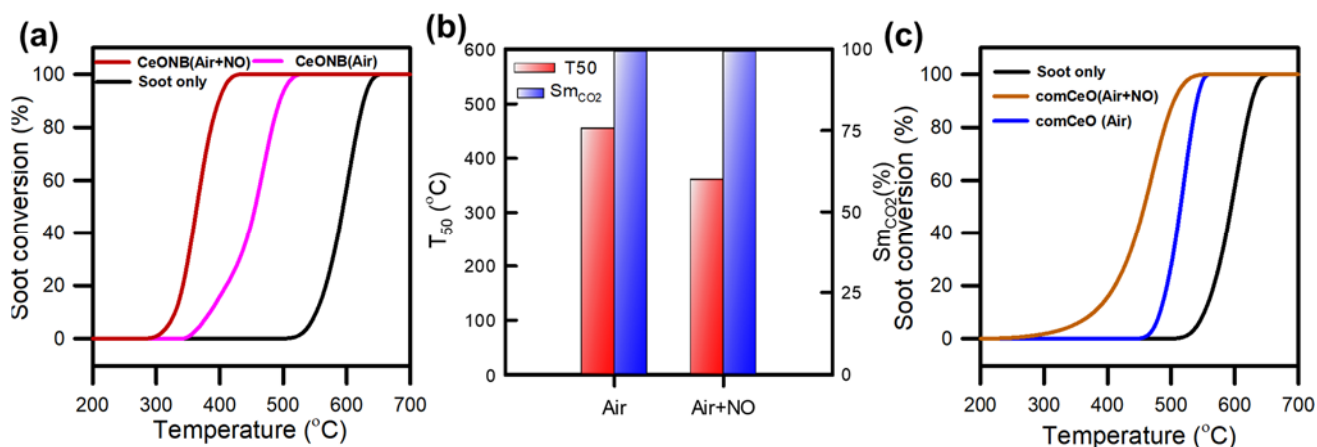


**Figure 10.** Effect of NO on soot oxidation by CeONB: (a) soot conversion (%) and (b)  $T_{50}$  and  $S_{mCO_2}$ ; (c) the TPO profile of comCeO with/without NO.

In the absence of NO, the  $T_{ig}$  of CeONB was 352 °C, which was then noticeably reduced to 300 °C when NO was introduced in the feed gas.  $T_{50}$  by CeONB in the absence of NO was 456 °C, which was also considerably reduced to 363 °C in the presence of NO during the soot oxidation reaction (Figure 10b). Besides, soot conversion reached 100% at  $T_e = 432$  °C in the presence of NO, whereas  $T_e$  increased to 456 °C in absence of NO. These results indicated that the presence of NO seemed to enhance soot oxidation by CeONB, probably because the formation of active oxygen species induced by NO in the gas phase, thereby facilitating soot oxidation [35,36]. Besides, a synergic effect might also occur owing to decomposition of surface nitrate, which would result in gaseous  $NO_x$  and desorption of active oxygen. Such active oxygen species would then also assist soot oxidation [35,36].

To further demonstrate the pathway of such a NO-assisted process, and  $NO_x$  transformation, the in-situ DRIFTS was then adopted by introducing the mixture gas of  $NO+O_2$  at 350 °C into a reaction chamber at different times.

As displayed in Figure 11a, several peaks were quickly observed right after purging NO into the IR chamber, and intensities of these peaks increased gradually, then reaching the adsorption saturation after ca. 30 min. Specifically, the multiple peaks in the range of 800–2000  $\text{cm}^{-1}$ , which would be ascribed to bridging nitrate (ca. 1596, 1206, and 1001  $\text{cm}^{-1}$ ), bidentate nitrate (ca. 1556, 1270, and 1026  $\text{cm}^{-1}$ ), and monodentate nitrate (ca. 1535, 1243, and 1001  $\text{cm}^{-1}$ ), respectively [37,38]. Moreover, the peak at 1352  $\text{cm}^{-1}$  could be attributed to nitrite–nitrate on the  $\text{CeO}_2$  surface [38]. Moreover, the peaks of the chelated nitro compounds could also be detected at ca 1505 and 1243  $\text{cm}^{-1}$ , whereas the 1407  $\text{cm}^{-1}$  might be derived from the nitro compound [38].

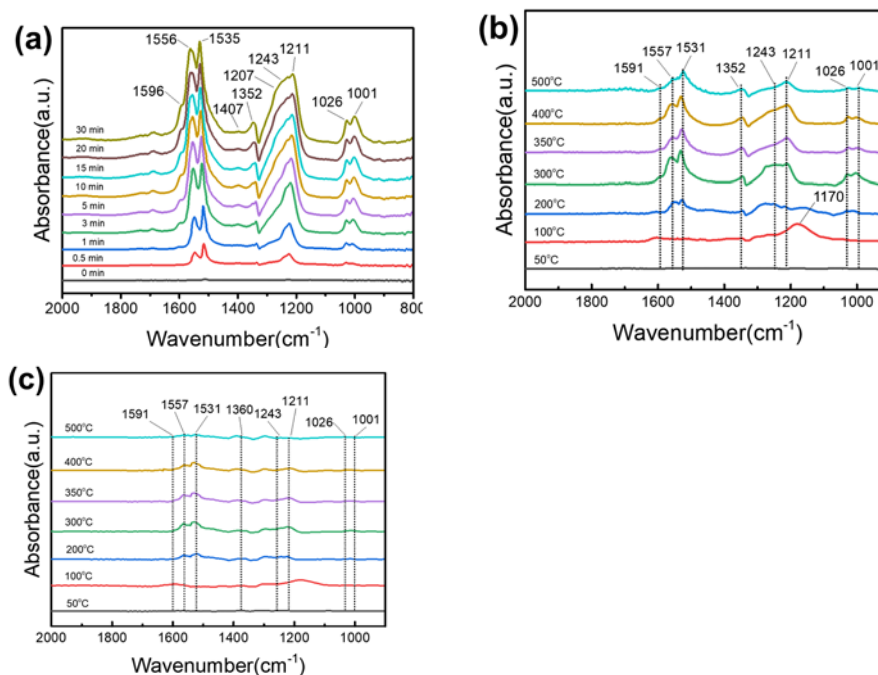


**Figure 11.** The in situ DRIFTS spectra of  $\text{NO}_x$  adsorption over  $\text{CeONB}$  at (a) different times (350 °C) and (b) different temperatures; (c) The in situ DRIFTS spectra of  $\text{NO}_x$  adsorption over  $\text{comCeO}$  at different temperatures.

On the other hand, DRIFT spectra at different temperatures were also obtained in Figure 11b, in which several peaks of nitrite (ca. 1211, 1170, and 1084  $\text{cm}^{-1}$ ) reached the adsorption saturation at 100 °C. After ramping the temperature to 250 °C, the intensity of nitrite bands gradually decreased, and then replaced by those bands of bidentate nitrates (1556, 1270, and 1001  $\text{cm}^{-1}$ ) and monodentate nitrates (1535, 1243, and 1001  $\text{cm}^{-1}$ ) [39].

In view of these observations, the decomposition of nitrate in the specific temperature range (e.g., 350–500 °C) would be very important for soot oxidation via such a  $\text{NO}_x$ -assisted process. These relatively stable nitrates would then react directly with carbon atoms nearby (Equation (1)) or decompose to release  $\text{NO}_2$  to react with soot (Equations (2) and (3)), together with the formation of  $\text{NO}$  as follows [39]:



Furthermore, the effect of  $\text{NO}$  on soot oxidation was also tested by using  $\text{comCeO}$ , as shown in Figure 10c, and the presence of  $\text{NO}$  also enhanced soot oxidation by decreasing  $T_{50}$  from 514 to 457 °C. Nevertheless, the  $\text{NO}$ -assisted enhancement in the case of  $\text{comCeO}$  was less than that in the case of  $\text{CeONB}$ . To further elucidate such a difference, DRIFTS

was also employed to determine the surface activity of comCeO in the presence of NO in Figure 11c. While the aforementioned nitrogen-containing intermediates could be still observed, intensities of these species detected were much lower than those detected in the case of CeONB. This indicates that CeONB certainly exhibited much higher surface activities to react with NO<sub>x</sub> than comCeO, thereby leading to a stronger NO-assisted enhancement.

### 2.5. Recyclability

While CeONB verified the highly catalytic activities for soot oxidation, it was essential to obtain its reusability over several cycles of using. Figure 12a indicated that it remained completed with 100% conversion over five cycles for soot oxidation by CeONB without regeneration treatments. In addition, the corresponding T<sub>50</sub> only slightly increased from 352–358 °C after five cycles.

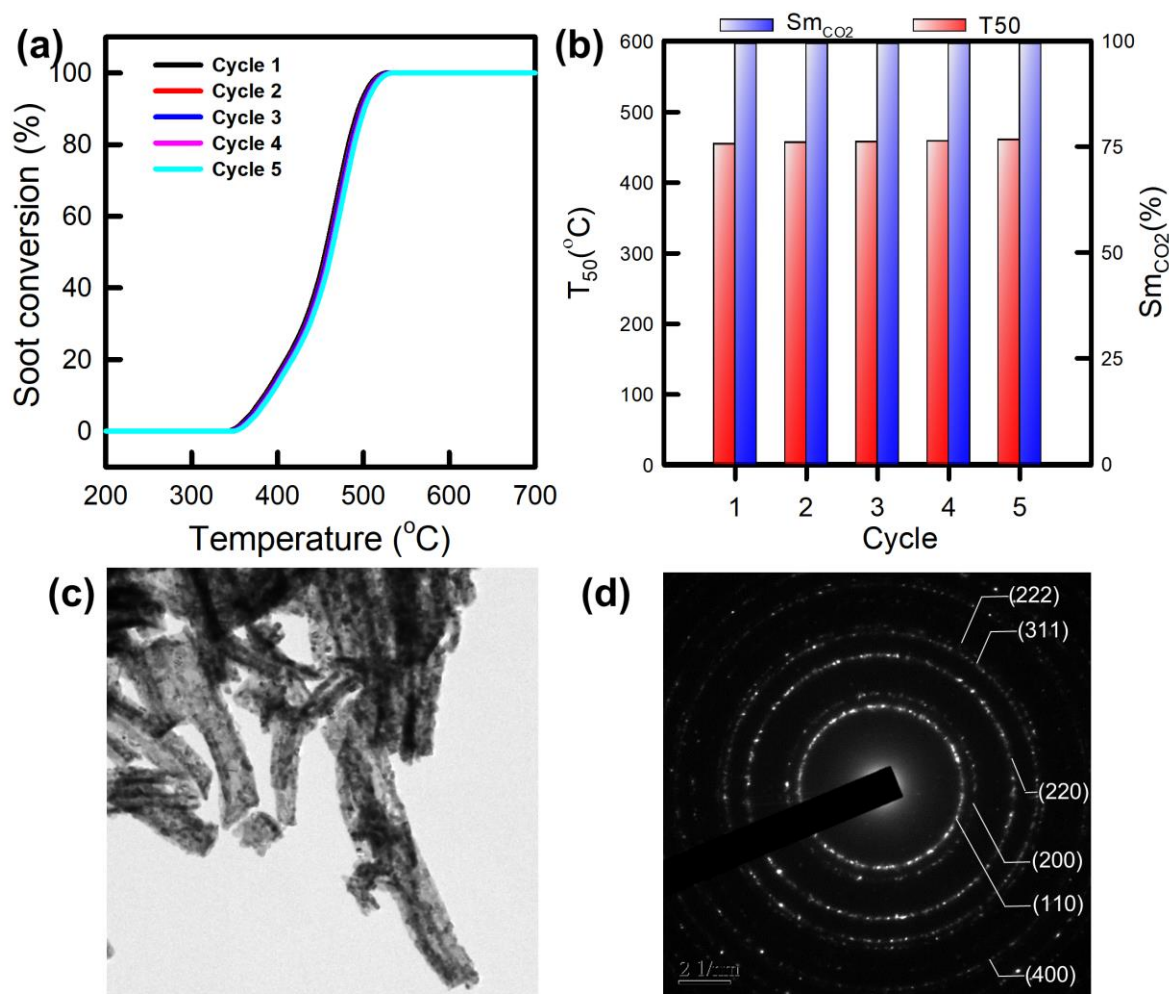


**Figure 12.** Recyclability of CeONB for multi-cycle soot oxidation: (a) soot conversion (%), (b) T<sub>m</sub> and S<sub>mCO2</sub>, and (c) XRD pattern of used CeONB; (d) SAED pattern of used CeONB.

Moreover, Figure 12b further shows the values of T<sub>m</sub> and S<sub>mCO2</sub> of five cycles, which displayed very similar over five cycles without notable changes. The results employed that CeONB could be effectively reused over five cycles for soot oxidation. Besides, T<sub>m</sub> and S<sub>mCO2</sub> values were also consistent over the consecutive five cycles without significant variations. This demonstrates that CeONB was reusable for catalytic soot oxidation, and its catalytic activity was consistent and efficient. In addition, the TEM image and SAED pattern of used CeONB (Figure 12c,d) were very comparable to those of the pristine CeONB, validating that CeONB was a durable and stable catalyst for soot oxidation.

### 3. Materials and Methods

#### 3.1. Materials

All chemicals involved in this study were commercially available and used as received without purification. Cerous nitrate hexahydrate and benzene-1,3,5-tricarboxylic acid (H<sub>3</sub>BTC) were purchased from Sigma-Aldrich (Burlington, MA, USA). Commercial CeO<sub>2</sub> nanoparticles (NPs) (comCeO) (purity  $\geq$  99.55%, 50–100 nm) were purchased from Echo Chemical Co. LTD (Taiwan). Carbon black pigment branded as Printex<sup>®</sup> U was employed as a model soot and it was supplied by Orion Engineered Carbon (Luxemburg). Acronyms and variables are listed in Table 4.

**Table 4.** The list of acronyms and variables.

MOFs	Metal Organic Frameworks
CeONB	CeO <sub>2</sub> nanobar
comCeO	commercial CeO <sub>2</sub> nanoparticle
NPs	nanoparticles
PDFs	diesel particulate filters
O <sub>lat</sub>	lattice oxygen
O <sub>vac</sub>	oxygen vacancy
O <sub>ab</sub>	absorbed oxygen species
F <sub>2g</sub>	the fluorite-type structure of CeO <sub>2</sub>
I <sub>D</sub>	correlated to the formation of oxygen vacancy
DRIFTS	Diffuse Reflectance Infrared Fourier Transform Spectroscopy
T <sub>ig</sub>	ignition temperature
T <sub>m</sub>	temperature at the maximum concentration of CO <sub>2</sub>
T <sub>50</sub> and T <sub>90</sub>	the temperature at which 50% and 90% of the soot conversion, respectively
T <sub>e</sub>	the temperature at which 100% of soot oxidation
S <sub>CO2</sub>	the CO <sub>2</sub> selectivity
S <sub>mCO2</sub>	the S <sub>CO2</sub> at T <sub>m</sub>

#### 3.2. Preparation and Characterization of CeONB

Preparation of CeONB can be schematically illustrated in Figure 1. Firstly, Ce-MOF with a bar-like morphology was synthesized through hydrothermal synthesis of coordinating Ce<sup>3+</sup> with H<sub>3</sub>BTC. Typically, 10 mmol (0.63 g) of H<sub>3</sub>BTC and 10 mmol (2.17 g) of Ce(NO<sub>3</sub>)<sub>3</sub> were dissolved in a mixture of ethanol/water (1:1) under vigorous stirring for 5 min. Next, the mixture was then left without stirring at 60 °C for 12h. Then, the yellowish precipitates were collected, washed with ethanol repeatedly, and dried at 80 °C overnight to afford Ce-MOF. The resulting bar-like Co-MOF was then calcined in air at 800 °C to generate CeO<sub>2</sub> with a bar-like morphology.

#### 3.3. Characterization

Materials used here were firstly characterized for their morphologies by SEM and TEM (JEOL JEM-2010, Tokyo, Japan). The selected area electron diffraction (SAED) pattern method was used for performing the TEM structural analysis.

The crystalline structures of the as-prepared materials were measured by an X-ray diffractometer (XRD) (Bruker D8, Billerica, MA, USA).

Surface chemistry of CeONB and comCeO was analyzed by X-ray Photoelectron Spectroscopy (PHI 5000, Kanagawa, Japan) to provide chemical states of different elements.

Thermo-gravimetric (TG) analyses were conducted using a TG analyzer (TGA i1000, ISI, USA) to verify the thermal stability the as-prepared catalysts.

Raman spectroscopic analyses of catalysts were performed by a Raman confocal spectroscopy (TII, Tokyo, Japan) to examine the surface structure of CeONB and comCeO as well as characterize the oxygen vacancy concentration.

The specific surface area, pore volume, and pore size distribution were obtained by the BET method using ANTON PAAR NOVATOUCHE LX2, Graz, Austria.

Textural properties, temperature-programmed reduction (TPR), and desorption (TPD) profiles of catalysts were measured by a volumetric gas adsorption analyzer equipped with a TCD detector (Anton Paar Quantachrome ASIQ, Graz, Austria).

### 3.4. Catalytic Oxidation of Soot

The catalytic activity of CeONB for soot oxidation was investigated by temperature-programmed oxidation (TPO) of soot in a fixed-bed tubular reactor. At first, air gas with 79.5 vol.% N<sub>2</sub> and 20.5 vol.% O<sub>2</sub> flew through a mixture of soot and catalyst (100 mg) (soot: catalyst = 1:9) at a rate of 100 mL/min. Subsequently, the tubular reactor would be heated from room temperature to 150 °C for 30 min to eliminate moisture, and absorbed hydrocarbons. Next, temperature would be ramped from 150–700 °C at a rate of 5 °C/min. For studying soot oxidation under different contact modes, the catalyst and soot would be mixed by a spatula to afford the loose contact mode, whereas the mixture would be ground in an agate mortar to provide the tight contact mode [23,29].

Concentrations of CO<sub>2</sub> and CO were measured using an infrared analyzer (Infrared Industries IR208, Hayward, CA, USA). For investigating effect of NO on feed gases on soot oxidation, a feed gas containing air and 500 ppm of NO was prepared and employed. Thermogravimetric analyses (TGA) were conducted in oxygen atmosphere on a thermogravimetric analyzer (TA Q50, New Castle, DE, USA).

### 3.5. Diffuse Reflectance Fourier Transform Spectroscopy (DRIFTS)

DRIFTS spectra were obtained using a FTIR spectrometer (JASCO 6800, Tokyo, Japan) with a MCT detector and a diffuse reflection accessory (Harrick Praying Mantis, Pleasantville, NY, USA). In a typical DRIFTS experiment, the catalyst was then placed into the heating chamber, purged with N<sub>2</sub> at 600 °C for 20 min, and then cooled down to 25 °C to eliminate the surface-adsorbed impurities (e.g., H<sub>2</sub>O and CO<sub>2</sub>) on catalyst surface. All spectra were measured by a scan rate of 32 with a resolution of 4 cm<sup>-1</sup> in the range from 1000 cm<sup>-1</sup> to 4000 cm<sup>-1</sup>.

## 4. Conclusions

In this study, a Ce-MOF consisting of Ce and H<sub>3</sub>BTC was employed as the precursor as CeBTC exhibited a high-aspect-ratio morphology which was transformed into CeO<sub>2</sub> with a nanoscale bar-like configuration. More importantly, the resulting CeO<sub>2</sub> nanobar (CeONB) exhibited porous, and even hollow structures, as well as more oxygen vacancies, enabling CeONB to become a promising catalyst for soot oxidation. Thus, CeONB showed a much higher catalytic activity than comCeO for soot oxidation with a much lower T<sub>ig</sub>. Moreover, while soot oxidation by comCeO led to production of CO together with CO<sub>2</sub>, CeONB was able to completely convert soot to CO<sub>2</sub>. The tight contact mode also enabled CeONB to exhibit a low T<sub>ig</sub> of 310 °C, whereas the presence of NO also enhanced the soot oxidation by CeONB to reduce the T<sub>ig</sub> and T<sub>m</sub>. The mechanism of NO-assisted soot oxidation was also investigated, and validated by DRIFTS to identify the formation and transformation of intermediates and elucidate differences of catalytic activities between CeONB and comCeO. CeONB was also recyclable over many consecutive cycles and maintained its high catalytic activity for soot oxidation. These results demonstrate that CeONB was a promising and easily prepared high-aspect-ratio Ce-based catalyst for soot oxidation.

**Supplementary Materials:** The following are available online at <https://www.mdpi.com/article/10.3390/catal11091128/s1>, Figure S1: (a,b) SEM images of commercial CeO<sub>2</sub> (comCeO).

**Author Contributions:** Conceptualization, Y.-C.T. and J.L.; methodology, E.K.; software, C.-W.H.; validation, W.D.O.; data curation, and P.-S.H. and N.N.H.; writing—original draft preparation, W.D.O.; writing—review and editing, K.-Y.A.L.; visualization, S.Y. All authors have read and agreed to the published version of the manuscript.

**Funding:** This work is supported by the Ministry of Science and Technology (MOST)(110-2636-E-005-003-), Taiwan, and financially supported by the “Innovation and Development Center of Sustainable Agriculture” from The Featured Areas Research Center Program within the framework of the Higher Education Sprout Project by the Ministry of Education (MOE), Taiwan.

**Data Availability Statement:** Not applicable.

**Conflicts of Interest:** The authors declare no conflict of interest.

## References

1. Fang, P.; Luo, M.-F.; Lu, J.-Q.; Cen, S.-Q.; Yan, X.-Y.; Wang, X.-X. Studies on the oxidation properties of nanopowder CeO<sub>2</sub>-based solid solution catalysts for model soot combustion. *Thermochim. Acta* **2008**, *478*, 45–50. [[CrossRef](#)]
2. Neeft, J.P.A.; van Pruissen, O.P.; Makkee, M.; Moulijn, J.A. Catalysts for the oxidation of soot from diesel exhaust gases II. Contact between soot and catalyst under practical conditions. *Appl. Catal. B* **1997**, *12*, 21–31. [[CrossRef](#)]
3. Stratakis, G.A.; Stamatelos, A.M. Thermogravimetric analysis of soot emitted by a modern diesel engine run on catalyst-doped fuel. *Combust. Flame* **2003**, *132*, 157–169. [[CrossRef](#)]
4. Fino, D.; Bensaid, S.; Piumetti, M.; Russo, N. A review on the catalytic combustion of soot in Diesel particulate filters for automotive applications: From powder catalysts to structured reactors. *Appl. Catal. A Gen.* **2016**, *509*, 75–96. [[CrossRef](#)]
5. van Setten, B.A.A.L.; Makkee, M.; Moulijn, J.A. Science and technology of catalytic diesel particulate filters. *Catal. Rev.* **2001**, *43*, 489–564. [[CrossRef](#)]
6. Gao, Y.; Duan, A.; Liu, S.; Wu, X.; Liu, W.; Li, M.; Chen, S.; Wang, X.; Weng, D. Study of Ag/Ce<sub>x</sub>Nd<sub>1-x</sub>O<sub>2</sub> nanocubes as soot oxidation catalysts for gasoline particulate filters: Balancing catalyst activity and stability by Nd doping. *Appl. Catal. B* **2017**, *203*, 116–126. [[CrossRef](#)]
7. Nanba, T.; Masukawa, S.; Abe, A.; Uchisawa, J.; Obuchi, A. Quantitative analysis of active oxygen for soot oxidation over Ag/ZrO<sub>2</sub>: Characterization with temperature-programmed reduction by NH<sub>3</sub>. *Appl. Catal. B* **2012**, *123–124*, 351–356. [[CrossRef](#)]
8. Nanba, T.; Masukawa, S.; Abe, A.; Uchisawa, J.; Obuchi, A. Morphology of active species of Ag/ZrO<sub>2</sub> for low-temperature soot oxidation by oxygen. *Catal. Sci. Technol.* **2012**, *2*, 1961–1966. [[CrossRef](#)]
9. Wu, S.; Yang, Y.; Lu, C.; Ma, Y.; Yuan, S.; Qian, G. Soot Oxidation over CeO<sub>2</sub> or Ag/CeO<sub>2</sub>: Influences of Bulk Oxygen Vacancies and Surface Oxygen Vacancies on Activity and Stability of the Catalyst. *Eur. J. Inorg. Chem.* **2018**, *2018*, 2944–2951. [[CrossRef](#)]
10. Neelapala, S.D.; Patnaik, H.; Dasari, H. Enhancement of soot oxidation activity of manganese oxide (Mn<sub>2</sub>O<sub>3</sub>) through doping by the formation of Mn<sub>1.9</sub>M<sub>0.1</sub>O<sub>3-δ</sub> (M = Co, Cu, and Ni). *Asia-Pac. J. Chem. Eng.* **2018**, *13*, e2234. [[CrossRef](#)]
11. Wagloehner, S.; Nitzer-Noski, M.; Kureti, S. Oxidation of soot on manganese oxide catalysts. *Chem. Eng. J.* **2015**, *259*, 492–504. [[CrossRef](#)]
12. Aneggi, E.; de Leitenburg, C.; Dolcetti, G.; Trovarelli, A. Promotion effect of surface Lanthanum in soot oxidation over ceria-based catalysts. *Top. Catal.* **2007**, *42*, 319–322. [[CrossRef](#)]
13. Nascimento, L.F.; Lima, J.F.; de Sousa Filho, P.C.; Serra, O.A. Effect of lanthanum loading on nanosized CeO<sub>2</sub>-ZnO solid catalysts supported on cordierite for diesel soot oxidation. *J. Environ. Sci.* **2018**, *73*, 58–68. [[CrossRef](#)] [[PubMed](#)]
14. Tsai, Y.-C.; Huy, N.N.; Tsang, D.C.W.; Lin, K.-Y.A. Metal organic framework-derived 3D nanostructured cobalt oxide as an effective catalyst for soot oxidation. *J. Colloid Interface Sci.* **2020**, *561*, 83–92. [[CrossRef](#)]
15. Tsai, Y.-C.; Nhat Huy, N.; Lee, J.; Lin, Y.-F.; Lin, K.-Y.A. Catalytic soot oxidation using hierarchical cobalt oxide microspheres with various nanostructures: Insights into relationships of morphology, property and reactivity. *Chem. Eng. J.* **2020**, *395*, 124939. [[CrossRef](#)]
16. Machida, M.; Murata, Y.; Kishikawa, K.; Zhang, D.; Ikeue, K. On the Reasons for High Activity of CeO<sub>2</sub> Catalyst for Soot Oxidation. *Chem. Mater.* **2008**, *20*, 4489–4494. [[CrossRef](#)]
17. Deng, X.; Li, M.; Zhang, J.; Hu, X.; Zheng, J.; Zhang, N.; Chen, B.H. Constructing nano-structure on silver/ceria-zirconia towards highly active and stable catalyst for soot oxidation. *Chem. Eng. J.* **2017**, *313*, 544–555. [[CrossRef](#)]
18. Shi, Q.; Liu, T.; Li, Q.; Xin, Y.; Lu, X.; Tang, W.; Zhang, Z.; Gao, P.-X.; Anderson, J.A. Multiple strategies to decrease ignition temperature for soot combustion on ultrathin MnO<sub>2-x</sub> nanosheet array. *Appl. Catal. B Environ.* **2019**, *246*, 312–321. [[CrossRef](#)]
19. Aneggi, E.; Wiater, D.; de Leitenburg, C.; Llorca, J.; Trovarelli, A. Shape-Dependent Activity of Ceria in Soot Combustion. *ACS Catal.* **2014**, *4*, 172–181. [[CrossRef](#)]
20. Miceli, P.; Bensaid, S.; Russo, N.; Fino, D. CeO<sub>2</sub>-based catalysts with engineered morphologies for soot oxidation to enhance soot-catalyst contact. *Nanoscale Res. Lett.* **2014**, *9*, 254. [[CrossRef](#)]
21. Piumetti, M.; Bensaid, S.; Russo, N.; Fino, D. Nanostructured ceria-based catalysts for soot combustion: Investigations on the surface sensitivity. *Appl. Catal. B Environ.* **2015**, *165*, 742–751. [[CrossRef](#)]
22. Zhang, W.; Niu, X.; Chen, L.; Yuan, F.; Zhu, Y. Soot Combustion over Nanostructured Ceria with Different Morphologies. *Sci. Rep.* **2016**, *6*, 29062. [[CrossRef](#)] [[PubMed](#)]
23. Bensaid, S.; Russo, N.; Fino, D. CeO<sub>2</sub> catalysts with fibrous morphology for soot oxidation: The importance of the soot-catalyst contact conditions. *Catal. Today* **2013**, *216*, 57–63. [[CrossRef](#)]
24. Lee, C.; Shul, Y.-G.; Einaga, H. Silver and manganese oxide catalysts supported on mesoporous ZrO<sub>2</sub> nanofiber mats for catalytic removal of benzene and diesel soot. *Catal. Today* **2017**, *281*, 460–466. [[CrossRef](#)]

25. Lee, Y.; He, G.; Akey, A.J.; Si, R.; Flytzani-Stephanopoulos, M.; Herman, I.P. Raman Analysis of Mode Softening in Nanoparticle  $\text{CeO}_2-\delta$  and  $\text{Au-CeO}_2-\delta$  during CO Oxidation. *J. Am. Chem. Soc.* **2011**, *133*, 12952–12955. [[CrossRef](#)]
26. Yap, M.H.; Fow, K.L.; Chen, G.Z. Synthesis and applications of MOF-derived porous nanostructures. *Green Energy Environ.* **2017**, *2*, 218–245. [[CrossRef](#)]
27. Zhang, X.; Hou, F.; Li, H.; Yang, Y.; Wang, Y.; Liu, N.; Yang, Y. A strawsheave-like metal organic framework Ce-BTC derivative containing high specific surface area for improving the catalytic activity of CO oxidation reaction. *Microporous Mesoporous Mater.* **2018**, *259*, 211–219. [[CrossRef](#)]
28. Zhang, X.; Hou, F.; Yang, Y.; Wang, Y.; Liu, N.; Chen, D.; Yang, Y. A facile synthesis for cauliflower like  $\text{CeO}_2$  catalysts from Ce-BTC precursor and their catalytic performance for CO oxidation. *Appl. Surf. Sci.* **2017**, *423*, 771–779. [[CrossRef](#)]
29. Zheng, X.; Li, Y.; Zhang, L.; Shen, L.; Xiao, Y.; Zhang, Y.; Au, C.; Jiang, L. Insight into the effect of morphology on catalytic performance of porous  $\text{CeO}_2$  nanocrystals for  $\text{H}_2\text{S}$  selective oxidation. *Appl. Catal. B Environ.* **2019**, *252*, 98–110. [[CrossRef](#)]
30. Chen, Z.; Chen, L.; Jiang, M.; Gao, X.; Huang, M.; Li, Y.; Ren, L.; Yang, Y.; Yang, Z. Controlled synthesis of  $\text{CeO}_2$  nanorods and their promotional effect on catalytic activity and aging resistibility for diesel soot oxidation. *Appl. Surf. Sci.* **2020**, *510*, 145401. [[CrossRef](#)]
31. Miceli, P.; Bensaid, S.; Russo, N.; Fino, D. Effect of the morphological and surface properties of  $\text{CeO}_2$ -based catalysts on the soot oxidation activity. *Chem. Eng. J.* **2015**, *278*, 190–198. [[CrossRef](#)]
32. Zhu, H.; Xu, J.; Yichuan, Y.; Wang, Z.; Gao, Y.; Liu, W.; Yin, H. Catalytic oxidation of soot on mesoporous ceria-based mixed oxides with cetyltrimethyl ammonium bromide (CTAB)-assisted synthesis. *J. Colloid Interface Sci.* **2017**, *508*, 1–13. [[CrossRef](#)] [[PubMed](#)]
33. Zouaoui, N.; Issa, M.; Kehrl, D.; Jeguirim, M.  $\text{CeO}_2$  catalytic activity for soot oxidation under  $\text{NO/O}_2$  in loose and tight contact. *Catal. Today* **2012**, *189*, 65–69. [[CrossRef](#)]
34. Christensen, J.M.; Grunwaldt, J.-D.; Jensen, A.D. Importance of the oxygen bond strength for catalytic activity in soot oxidation. *Appl. Catal. B* **2016**, *188*, 235–244. [[CrossRef](#)]
35. Setiabudi, A.; Van Setten, B.A.; Makkee, M.; Moulijn, J.A. The influence of  $\text{NO}_x$  on soot oxidation rate: Molten salt versus platinum. *Appl. Catal. B Environ.* **2002**, *35*, 159–166. [[CrossRef](#)]
36. Jelles, S.; Krul, R.; Makkee, M.; Moulijn, J.A. The influence of  $\text{NO}_x$  on the oxidation of metal activated diesel soot. *Catal. Today* **1999**, *53*, 623–630. [[CrossRef](#)]
37. Hadjiivanov, K.I. Identification of Neutral and Charged  $\text{N}_x\text{O}_y$  Surface Species by IR Spectroscopy. *Catal. Rev.* **2000**, *42*, 71–144. [[CrossRef](#)]
38. Setiabudi, A.; Chen, J.; Mul, G.; Makkee, M.; Moulijn, J.A.  $\text{CeO}_2$  catalysed soot oxidation: The role of active oxygen to accelerate the oxidation conversion. *Appl. Catal. B* **2004**, *51*, 9–19. [[CrossRef](#)]
39. Wu, X.; Liu, S.; Lin, F.; Weng, D. Nitrate storage behavior of  $\text{Ba/MnO}_x\text{-CeO}_2$  catalyst and its activity for soot oxidation with heat transfer limitations. *J. Hazard. Mater.* **2010**, *181*, 722–728. [[CrossRef](#)]